

# The Palletrone Cart: Human-Robot Interaction-Based Aerial Cargo Transportation

Geonwoo Park<sup>1</sup>, Hyungeun Park<sup>1</sup>, Wooyong Park<sup>1</sup>, Dongjae Lee<sup>2</sup>, *Graduate Student Member, IEEE*,  
Murim Kim<sup>3</sup>, *Senior Member, IEEE* and Seung Jae Lee<sup>1</sup>, *Member, IEEE*

**Abstract**—This paper presents a new cargo transportation solution based on physical human-robot interaction utilizing a novel fully-actuated multirotor platform called Palletrone. The platform is designed with a spacious upper flat surface for easy cargo loading, complemented by a rear-mounted handle reminiscent of a shopping cart. Flight trajectory control is achieved by a human operator gripping the handle and applying three-dimensional forces and torques while maintaining a stable cargo transport with zero roll and pitch attitude throughout the flight. To facilitate physical human-robot interaction, we employ an admittance control technique. Instead of relying on complex force estimation methods, like in most admittance control implementations, we introduce a simple yet effective estimation technique based on a disturbance observer robust control algorithm. We conducted an analysis of the flight stability and performance in response to changes in system mass resulting from arbitrary cargo loading. Ultimately, we demonstrate that individuals can effectively control the system trajectory by applying appropriate interactive forces and torques. Furthermore, we showcase the performance of the system through various experimental scenarios.

**Index Terms**—APhI, admittance control, disturbance observer, aerial transportation, physical human-robot interaction

## I. INTRODUCTION

MULTIROTOR unmanned aerial vehicles (mUAVs) have evolved beyond conventional “aerial imaging” platforms [1] and are becoming versatile robotic platforms for transporting cargo [2] and mission equipment, leveraging their three-dimensional motion capabilities. In particular, there is a growing focus on “Aerial Physical Interaction (APhI)” missions, where a fuselage or attached robotic manipulators are utilized for physical interactions with external objects [3], [4]. Notably, physical Human-Robot Interaction (pHRI) missions,



Fig. 1. Cargo transportation based on pHRI with the Palletrone mUAV. Human operators can load cargo onto the upper surface of the platform, similar to a conventional shopping cart, and then apply force and torque through the handrail to control horizontal, vertical, and yaw motion trajectories.

emphasizing collaboration between mUAV robots and humans [5]–[8], have been gaining much attention.

As emphasized in [8], one primary objective of multirotor pHRI is to achieve flight control through physical interaction with the human operator. This concept involves individuals exerting force directly on the platform to steer its motion, thereby altering the flight path as the operator intended and eliminating the need for complex autonomous path planning algorithms. For this, a novel and intuitive cargo transportation technique can be designed and utilized. Similar to manipulating a cart in a shopping mall, cargo can be placed on a dedicated cargo bay and the motion of the mUAV can be controlled by pHRI. This approach allows for intuitive and interactive aerial cargo transport, proving valuable for last-mile parcel delivery, shopping malls, and factory settings. Since the mUAV platform hovers without direct contact with the ground, this approach offers significant advantages, especially in challenging environments like stairs or unpaved terrains, where conventional wheeled carts encounter difficulties.

So far, the methods for pHRI with mUAVs involve the use of tethers [5], [6] or direct contact between the human body and hardware [7], [8]. Tether-based interaction, in particular, has garnered recent attention for its ability to enable force interaction at safe distances while directly applying force to the center of mass of the mUAV platform. However, this approach has limitations, as it only allows force interaction when the human pulls the mUAV, or vice versa. In contrast, directly gripping the fuselage to implement pHRI enables bi-directional interaction for both pushing and pulling. Nevertheless, this approach also presents challenges, including the potential risk of bodily harm from exposed rotor blades and interference with critical attitude control of mUAV flight, stemming from mechanical constraints imposed by human-body contact.

To overcome this issue, in this study, we introduce a novel aerial cargo transportation solution based on pHRI,

Manuscript received: February 20, 2024; Revised May 7, 2024; Accepted May 31, 2024.

This paper was recommended for publication by Editor Giuseppe Loianno upon evaluation of the Associate Editor and Reviewers’ comments. This study was financially supported by Seoul National University of Science & Technology.

<sup>1</sup>Geonwoo Park, Hyungeun Park, Wooyong Park and Seung Jae Lee are with the Department of Mechanical System Design Engineering, Seoul National University of Science and Technology (SeoulTech), Seoul 01811, Republic of Korea {kennethdhd1, dodoul, wy1004cow, seungjae\_lee}@seoultech.ac.kr

<sup>2</sup>Dongjae Lee is with the Department of Aerospace Engineering, Seoul National University (SNU), and Automation and Systems Research Institute (ASRI), Seoul 08826, Republic of Korea ehdwo713@snu.ac.kr

<sup>3</sup>Murim Kim is with the Human-centered Robotics R&D Division, Korea Institute of Robotics & Technology Convergence (KIRO), Pohang 37666, Republic of Korea mulimkim@kiro.re.kr

Digital Object Identifier (DOI): see top of this page.

as illustrated in Fig. 1. Our research includes innovative flight hardware for human-robot interaction and stable cargo conveyance, alongside a new pHRI flight controller design. For the dedicated mUAV platform design, we introduce Palletrone, a portmanteau of cargo ‘Pallet’ and ‘Drone,’ a purpose-built mUAV platform for this application. Unlike conventional mUAVs, Palletrone boasts redundant actuators for fully-actuated flight, enabling independent control of both rotational and translational motion [9]. This capability enhances stability during human-UAV interaction and cargo transportation by allowing the vehicle orientation to remain stationary throughout the flight. For pHRI flight control, we employ a compliance control algorithm commonly used in human-robot interaction for robotic manipulators [10]–[12]. This algorithm addresses the challenge of human-exerted forces causing deviations from the desired trajectory while simultaneously impeding the platform’s motion. As with other robotics applications, operating the compliance controller in mUAVs requires estimating external forces first because the control system aims to adapt the robot’s trajectory to these forces. Typically, other research in this area involves using F/T sensors [13], [14], or integrating separate estimators [8], [20], [21]. Moreover, compliance control for mUAVs requires robust control because external forces directly induce system motion even before control is applied, unlike most ground-based robotic manipulators, which exhibit low backdrivability. In our research, we introduce a new approach by incorporating a Disturbance Observer (DOB) robust control algorithm into the mUAV compliance controller [15], [16]. This new approach not only provides robust motion control performance against human-induced forces but also enables pHRI force estimation through a single DOB algorithm, without the need for additional estimation algorithms or sensors. This unified method simplifies the control system setup, facilitates stability and performance evaluations, and offers a computationally light compliance control structure compared to some estimator-integrated algorithms, particularly those based on optimization [20]. Assigning a new goal of pHRI wrench estimation to the DOB is a unique feature of this paper and represents one of the primary contributions of this research.

This paper is structured as follows: Section II provides an overview of the hardware structure and dynamics of the Palletrone mUAV platform, Section III introduces a new compliance control approach utilizing the DOB algorithm, along with stability and performance analysis, Section IV presents experimental results validating flight performance, and Section V concludes the paper.

## II. THE PALLETRONE FLIGHT PLATFORM

In this section, we present an overview of the Palletrone hardware for aerial pHRI cargo transportation, followed by an introduction to the dynamics of the aircraft.

### A. Hardware design

Fig. 2 displays the detailed hardware configuration, featuring a cubic, porous panel enclosure to prevent human body contact with the propellers while allowing sufficient airflow for

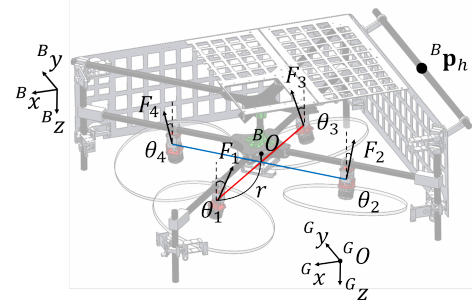


Fig. 2. The Palletrone mUAV hardware consists of a cuboid-shaped body enclosed by a porous structure. Inside, four propeller propulsion systems facilitate thrust vectoring. The human operator manipulates the trajectory by applying force and torque through a handle assumed to act at  ${}^B\mathbf{p}_h$ .

propulsion. The upper section has a flat surface for convenient cargo loading, providing a more flexible solution compared to traditional cargo bays beneath the fuselage. The internal structure comprises an X-shaped frame with arms, each equipped with a propeller propulsion system and servo motors for thrust vectoring. This redundant system consists of eight actuators: four propellers generating forces  $F_{\{1,2,3,4\}} \in \mathbb{R}$  and four servo motors controlling thrust vector angles  $\theta_{\{1,2,3,4\}} \in \mathbb{R}$ . A rear handrail facilitates physical interaction, allowing users to apply translational motion forces and adjust the orientation of the cart.

By leveraging eight actuators, we can independently control the three-dimensional propulsion force vector  ${}^B\mathbf{F}_p = [F_{p,x} \ F_{p,y} \ F_{p,z}]^T \in \mathbb{R}^{3 \times 1}$  and attitude control torque vector  ${}^B\mathbf{T}_p = [\tau_{p,x} \ \tau_{p,y} \ \tau_{p,z}]^T \in \mathbb{R}^{3 \times 1}$ , achieving fully-actuated six-degrees-of-freedom flight. Stable cargo transportation is ensured by maintaining constant roll and pitch attitudes throughout the pHRI transportation flight, utilizing the platform’s fully-actuated flight capability.

The prototype of the Palletrone design and its basic flight control algorithm was first introduced in [17]. In this study, we utilize previous research results to execute basic flight, including generating accurate forces and torques for precise flight control. However, our new Palletrone platform has undergone hardware modifications for pHRI, including an increase in actuators from 6 to 8, a revised thrust vectoring mechanism, and an enlarged platform size for enhanced cargo loading capacity. The addition of a handrail for pHRI distinguishes it from the previous platform.

### B. Dynamics

Palletrone is characterized by a fixed hardware structure for most components, excluding propeller and servo motors, which constitute a relatively small portion of its overall mass. This characteristic facilitates its interpretation as a single rigid body. Moreover, independently generating force and torque wrenches enables a separate operation of both translational and rotational motion. In the end, the motion can be modeled as follows according to the established dynamics commonly associated with mUAVs:

$$\begin{cases} {}^G R_B(\mathbf{q}) {}^B \mathbf{F} = m {}^G \ddot{\mathbf{X}} - m \mathbf{g} \\ {}^B \mathbf{T} = J^B \dot{\boldsymbol{\Omega}} + {}^B \boldsymbol{\Omega} \times J^B \boldsymbol{\Omega} \end{cases}, \quad (1)$$

where

$$\begin{cases} {}^B\mathbf{F} = {}^B\mathbf{F}_p + {}^B\mathbf{E}_f \\ {}^B\mathbf{T} = {}^B\mathbf{T}_p + {}^B\mathbf{E}_t, \end{cases} \quad \begin{cases} {}^B\mathbf{E}_f = {}^B\mathbf{H}_f \\ {}^B\mathbf{E}_t = {}^B\mathbf{H}_t + ({}^B\mathbf{p}_h - {}^B\mathbf{p}_c) \times {}^B\mathbf{H}_f. \end{cases} \quad (2)$$

Here,  ${}^G R_B(\mathbf{q}) \in SO(3)$  denotes the rotation matrix from the body to global coordinates, while  $\mathbf{q} = [\phi \ \theta \ \psi]^T \in \mathbb{R}^{3 \times 1}$  represents the orientation of the fuselage.  ${}^B\mathbf{F} \in \mathbb{R}^{3 \times 1}$  and  ${}^B\mathbf{T} \in \mathbb{R}^{3 \times 1}$  represent the final force and torque wrench, respectively, applied to the system. The variable  $m \in \mathbb{R}$  signifies the mass of the body,  ${}^G\mathbf{X} = [x \ y \ z]^T \in \mathbb{R}^{3 \times 1}$  stands for the global position vector of the platform, and  $\mathbf{g} = [0 \ 0 \ g]^T \in \mathbb{R}^{3 \times 1}$  represents the gravitational acceleration.  $J = \text{diag}(J_1, J_2, J_3) \in \mathbb{R}^{3 \times 3}$  is the moment of inertia tensor of the platform and  ${}^B\mathbf{E}_f = [e_{f,x} \ e_{f,y} \ e_{f,z}]^T \in \mathbb{R}^{3 \times 1}$  and  ${}^B\mathbf{E}_t = [e_{t,x} \ e_{t,y} \ e_{t,z}]^T \in \mathbb{R}^{3 \times 1}$  are lumped representations of the external force/torque component. Inside  ${}^B\mathbf{E}_f$  and  ${}^B\mathbf{E}_t$ ,  ${}^B\mathbf{H}_f = [f_{ho,x} \ f_{ho,y} \ f_{ho,z}]^T \in \mathbb{R}^{3 \times 1}$  and  ${}^B\mathbf{H}_t = [\tau_{ho,x} \ \tau_{ho,y} \ \tau_{ho,z}]^T \in \mathbb{R}^{3 \times 1}$  correspond to the force and torque wrenches exerted on the system by the human operator through pHRI.  ${}^B\mathbf{p}_h = [x_h \ y_h \ z_h]^T \in \mathbb{R}^{3 \times 1}$  represents the center position of the handle where pHRI wrenches are assumed to be concentrated and applied.  ${}^B\mathbf{p}_c = [x_c \ y_c \ z_c]^T \in \mathbb{R}^{3 \times 1}$  is the center of mass (CoM) position.

In Equation (2),  ${}^B\mathbf{E}_f$  only includes the force exerted by the human operator, while  ${}^B\mathbf{E}_t$  encompasses not only the torque directly applied but also the torque resulting from the force exerted by the operator due to the displacement between the center of gravity and the handle. However, some elements in  ${}^B\mathbf{E}_t$  are so small that they can be ignored.  $\tau_{ho,y}$  remains zero unless the operator intentionally twists the handle harshly along its axis, which is unusual. Additionally, as the magnitudes of the moment arm  $({}^B\mathbf{p}_h - {}^B\mathbf{p}_c)$  in the y- and z-directions are much smaller compared to the x-direction moment arm, we can ignore the effect of forces corresponding to those moment arms in pHRI torque assessment. Then, we can approximate  ${}^B\mathbf{E}_t$  as follows:

$${}^B\mathbf{E}_t = \begin{bmatrix} e_{t,x} \\ e_{t,y} \\ e_{t,z} \end{bmatrix} \approx \begin{bmatrix} \tau_{ho,x} \\ -(x_h - x_c)f_{ho,z} \\ \tau_{ho,z} + (x_h - x_c)f_{ho,y} \end{bmatrix}. \quad (3)$$

Among the components of  ${}^B\mathbf{E}_t$ , yaw torque  $e_{t,z}$  consists of two components: the yaw torque generated by the difference in force between the two hands gripping the handle ( $\tau_{ho,z}$ ) and the torque induced by the overall force in the y-direction ( $(x_h - x_c)f_{ho,y}$ ). However, because both components are produced by the physical interactions of human operators, we can treat  $e_{t,z}$  as the final overall yaw pHRI torque resulting from human intentions, without differentiating the individual elements within  $e_{t,z}$ . Hence, from a control standpoint, we can consider the components of  $e_{t,z}$  indiscriminately as lumped into a single element.

### III. DISTURBANCE OBSERVER-BASED COMPLIANT FLIGHT ALGORITHM

In this section, we introduce a pHRI flight control strategy utilizing the Palletrone platform. Initially, we present the application of the DOB algorithm to ensure the robustness

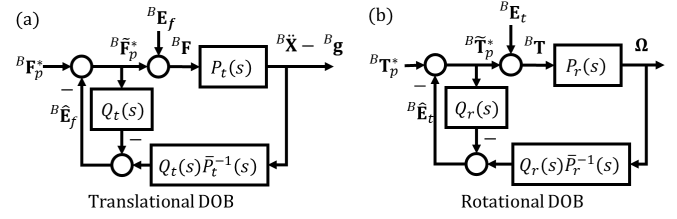


Fig. 3. Structures of the DOB algorithm for overcoming disturbances caused by  ${}^B\mathbf{E}_f$  and  ${}^B\mathbf{E}_t$ . In the DOB process, disturbances are estimated by comparing the actual and estimated target commands, and then compensated by incorporating these estimations into the next signal generation.

of flight concerning the pHRI wrenches exerted by the human operator on the aircraft. We then provide details regarding a compliant pHRI flight control algorithm utilizing the DOB robust controller. Finally, a brief analysis of the stability and performance of the proposed pHRI flight system is conducted.

#### A. Disturbance observer

In upcoming pHRI flight procedures, the human operator manipulates the aircraft by exerting force and torque, influencing the flight trajectory. However, Equation (2) reveals that these forces not only serve as inputs for the compliance controller but also directly influences the unintended effects on the control wrench generation. Thus, strategies to minimize the effect of disturbance of  ${}^B\mathbf{E}_f$  and  ${}^B\mathbf{E}_t$  on the control wrench generation must first be explored to govern accurate Palletrone motion control.

Fig. 3 illustrates the configurations of the DOB algorithm designed to mitigate the impacts of  ${}^B\mathbf{E}_f$  and  ${}^B\mathbf{E}_t$ . In the case of translational motion, which is shown in Fig. 3-(a), we define the relationship between the input force and output acceleration as  $P_t(s) = 1/m$ . We then estimate the resultant force  ${}^B\mathbf{F}$  applied to the system by inputting the measured acceleration values into the nominal model inverse of  $P_t(s)$ . Subsequently, the estimate is compared with the final desired force command  ${}^B\tilde{\mathbf{F}}_p^*$  to estimate  ${}^B\mathbf{E}_f$ . In reality, the acceleration of the platform is measured as a form of  ${}^B\ddot{\mathbf{X}} - {}^B\mathbf{g}$  through the Inertial Measurement Unit (IMU) sensor [18]. Then, with Equation (1), we can set the nominal model  $\tilde{P}_t(s)$  as  $1/\tilde{m}$ , where  $\tilde{m}$  represents the nominal mass of the fuselage without a cargo payload. To ensure a strictly proper DOB estimation process, we have the flexibility to select a  $Q_t(s) = \text{diag}(Q_t^h(s), Q_t^h(s), Q_t^v(s))$  low-pass filter with a relative degree of 1 or higher, incorporating horizontal and vertical components [19]. Then, by leveraging the structure depicted in the figure, we can estimate  ${}^B\tilde{\mathbf{E}}_f$  for generating modified control input  ${}^B\tilde{\mathbf{F}}_p^* = {}^B\mathbf{F}_p^* - {}^B\tilde{\mathbf{E}}_f$  including a disturbance compensation signal. Here, the asterisk superscript denotes the reference value generated by the high-level controller.

For rotational motion, shown in Fig. 3-(b), the measurement of angular acceleration is not achievable due to the inherent properties of an IMU, while the measurement of angular velocity remains possible. Moreover, given the static attitude, which is supposed to be consistently maintained in our proposed cargo transport scenarios, the term  ${}^B\boldsymbol{\Omega} \times J^B\boldsymbol{\Omega}$  in the rotational dynamics in Equation (1) becomes

negligible. Therefore, the ultimate expression for  $P_r(s) = \text{diag}(P_{r1}(s), P_{r2}(s), P_{r3}(s))$ , the relationship between torque input and the body angular speed, can be simplified to  $\text{diag}(1/(J_1s), 1/(J_2s), 1/(J_3s))$  and  $\bar{P}_r(s)$  becomes the replacement of each moment of inertia into  $\bar{J}_{\{1,2,3\}}$ , respectively. In this case, the  $Q_r(s) = \text{diag}(Q_r^r(s), Q_r^p(s), Q_r^y(s))$  low-pass filter, incorporating roll, pitch, and yaw components, must have a relative degree of 2 or higher for a strictly proper DOB estimation process. Then, identical to the case of translational DOB, we can generate modified control input  ${}^B\tilde{\mathbf{T}}_p^* = {}^B\mathbf{T}_p^* - \hat{\mathbf{E}}_t$ .

In conclusion, a well-designed DOB can yield the following outcomes in wrench control, aligning the final force and torque closely with the desired values:

$$\begin{cases} {}^B\mathbf{F} = {}^B\tilde{\mathbf{F}}_p^* + {}^B\mathbf{E}_f = {}^B\mathbf{F}_p^* + ({}^B\mathbf{E}_f - {}^B\hat{\mathbf{E}}_f) \approx {}^B\mathbf{F}_p^* \\ {}^B\mathbf{T} = {}^B\tilde{\mathbf{T}}_p^* + {}^B\mathbf{E}_t = {}^B\mathbf{T}_p^* + ({}^B\mathbf{E}_t - {}^B\hat{\mathbf{E}}_t) \approx {}^B\mathbf{T}_p^* \end{cases} \quad (4)$$

### B. Compliant pHRI Flight Control

For Palletrone's pHRI compliance control, we implement the Admittance control technique [8], [11]. Among the various compliance control methods, Admittance control [12] stands out for its ability to utilize existing motion controllers. It requires only additional controllers at the forefront of the existing control algorithm, along with an external force estimator, to regulate the desired trajectory and modify the force-response characteristics of the overall system. Given the intricate tuning processes for the translational and rotational motion controllers of mUAVs to ensure flight stability and performance, maintaining these existing motion controllers during the compliance controller design process is beneficial.

1) *Admittance control*: Based on [8], the transfer function of the admittance controller for adjusting the target reference trajectory solely by external force can be depicted as follows.

$$K_{adm}(s) = \frac{\Lambda_r(s)}{\hat{F}(s)} = \frac{1}{M_a s^2 + D_a s} \quad (5)$$

Here,  $\hat{F}(s)$  indicates the estimated external force/torque wrench exerted by the human operator for pHRI,  $\Lambda_r(s)$  refers to the target flight trajectory produced by the admittance controller, and  $M_a$  and  $D_a$  are the tunable virtual inertia and damping coefficients used to define the admittance motion characteristics.

As indicated in Equation (5), the successful operation of the admittance controller necessitates the estimation of  $F$ , representing the estimation of  ${}^B\mathbf{H}_{\{f,t\}}$  in the context of the Palletrone pHRI mission. Traditional estimation algorithms, such as Kalman Filters [8], dynamics-based [21], and Moving Horizon Estimators [20] have been employed for estimating external force/torque wrenches. However, the introduction of separate estimation algorithms can increase the complexity of the controller's overall structure, potentially leading to an increase in system tuning variables and complicating the analysis of performance and stability. In this context, we can leverage the DOB algorithm, which we have already utilized in our research. By employing existing algorithms, we can simplify

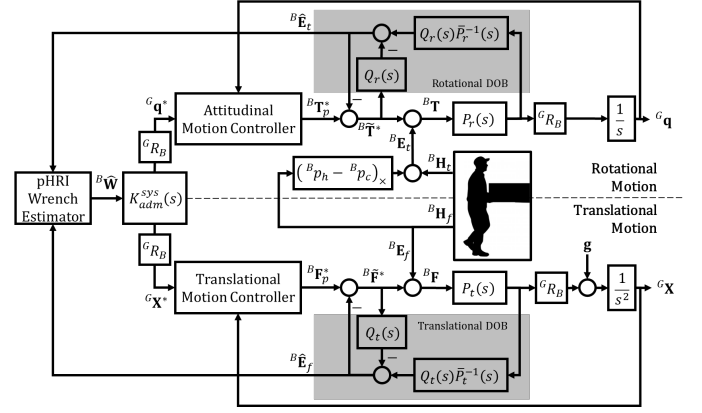


Fig. 4. The overall controller structure of the proposed admittance flight control technique. The admittance controller  $K_{adm}^{sys}(s)$  adjusts the reference trajectory based on the pHRI wrench inputs. Signals  ${}^B\hat{\mathbf{E}}_f$  and  ${}^B\hat{\mathbf{E}}_t$  from the DOB shown in Fig. 3 are utilized to estimate the pHRI wrench.

the controller structure, facilitate easy system setup through the reduction of tuning parameters, and enable straightforward stability and performance analysis. Therefore, we introduce DOB-based admittance control for pHRI interaction in the following.

2) *Admittance control with disturbance observer*: Fig. 4 depicts the proposed pHRI flight control algorithm. The upper segment along the central division line of the figure signifies the rotational motion system, while the lower segment represents the translational motion system. The block in the center of the figure represents the human operator; from this,  ${}^B\mathbf{H}_t$  and  ${}^B\mathbf{H}_f$  are introduced to the system.

Through the forthcoming pHRI wrench estimator, we first estimate the pHRI wrench  ${}^B\mathbf{W} = [{}^B\mathbf{H}_f^T \ e_{t,z}]^T \in \mathbb{R}^{4 \times 1}$ , where  ${}^B\mathbf{H}_f$  is for controlling three-dimensional translational motion and  $e_{t,z}$  is for controlling yaw motion. Then, the reference trajectory is generated by passing the following admittance controller:

$$K_{adm}^{sys}(s) = \text{diag}(K_{adm}^h(s), K_{adm}^h(s), K_{adm}^v(s), K_{adm}^y(s)). \quad (6)$$

Here,  $K_{adm}^h(s)$  represents the horizontal,  $K_{adm}^v(s)$  represents the vertical, and  $K_{adm}^y(s)$  represents the yaw orientation admittance controller, in accordance with the structure outlined in Equation (5). The reference trajectory generated is then subjected to a rotation matrix transformation, yielding  ${}^G\mathbf{q}^*$  and  ${}^G\mathbf{x}^*$ , while the desired roll and pitch attitude is set to be zero. Then, the reference trajectory passes through attitudinal and translational motion controller structures. These control systems feature dual feedback loops, including a translational position controller  $K_{tp}(s) = \text{diag}(K_{tp}^h(s), K_{tp}^h(s), K_{tp}^v(s))$  and a translational velocity controller  $K_{tv}(s) = \text{diag}(K_{tv}^h(s), K_{tv}^h(s), K_{tv}^v(s))$  for managing translation, along with an attitude controller  $K_{rp}(s) = \text{diag}(K_{rp}^r(s), K_{rp}^p(s), K_{rp}^y(s))$  and an angular velocity controller  $K_{rv}(s) = \text{diag}(K_{rv}^r(s), K_{rv}^p(s), K_{rv}^y(s))$  for rotation. Each of these four controllers operates based on PID feedback principles. These controllers, pre-defined to ensure a stable flight, facilitate the transformation into  ${}^B\mathbf{T}_p^*$  and  ${}^B\mathbf{F}_p^*$  desired control wrench signals, and undergoes the

DOB structure illustrated in Fig. 3 to determine the final pose of the Palletrone.

During the control process, leveraging the assistance of DOB allows us to reduce the impact of  ${}^B\mathbf{E}_t$  and  ${}^B\mathbf{E}_f$  when applying torque and force commands to the plant. Meanwhile, considering the close relationship between  ${}^B\mathbf{E}_f$ ,  ${}^B\mathbf{E}_t$  and  ${}^B\mathbf{H}_f$ ,  ${}^B\mathbf{H}_t$ , as evident from Equation (2), we utilize the internal  ${}^B\hat{\mathbf{E}}_f$  and  ${}^B\hat{\mathbf{E}}_t$  signal estimation process of DOB for conducting pHRI wrench estimation. However, we must first consider the case where the actual plant may severely differ from the nominal plant when cargo is loaded, since this research aims for cargo transport through the Palletrone.

When the cargo is loaded, the platform experiences an additional vertical force due to the gravitational pull of the cargo. Then, the system experiences additional disturbance force  $(m - \bar{m})\mathbf{g}$  along original  ${}^B\mathbf{E}_f$ , and the external force estimation of the translational DOB according to Fig. 3-(a) becomes as follows.

$${}^B\hat{\mathbf{E}}_f(s) = \frac{Q_t(s) \left( \left( \frac{\bar{m}}{m} - 1 \right) {}^B\mathbf{F}_p^*(s) + \frac{\bar{m}}{m} ({}^B\mathbf{E}_f + (m - \bar{m})\mathbf{g}) \right)}{1 + Q_t(s) \left( \frac{\bar{m}}{m} - 1 \right)} \quad (7)$$

In an ideal environment where  $\bar{m} = m$  ( $\bar{P}_t(s) = P_t(s)$ ), our original expectation is that  ${}^B\hat{\mathbf{E}}_f(s) = Q_t(s) {}^B\mathbf{E}_f$ . However, this assumption is not valid when cargo is added since  $m \neq \bar{m}$ , necessitating a thorough analysis to grasp its impact on final admittance control. This aspect is further explained in the subsequent subsections focusing on stability and performance. Meanwhile, since the Palletrone maintains a constant attitude during the flight,  $(m - \bar{m})\mathbf{g}$  can be replaced with  $(m - \bar{m})\mathbf{g}$ , and in this case, cargo gravity becomes a static force. Then, considering the static nature of the cargo gravity force, the ultimate additional force exerted by cargo gravity on  ${}^B\hat{\mathbf{E}}_f(s)$  becomes  $(m - \bar{m})\mathbf{g}$  when applying  $Q_t(j\omega(=0)) = 1$ ; a case of constant signal input, with the assumption that the Q filter is designed with a DC gain of 1. This result means that gravity consistently and constantly generates inadvertent external force estimations along the global z-direction in scenarios where stable zero-roll-pitch regulation is achieved. Consequently, in admittance control situations where a payload is present but no pHRI wrench is applied, the system is incapable of hovering and experiences a constant decline in altitude along the z-direction. Hence, an alternative approach must be considered for estimating  $f_{ho,z}$ .

An effective method for estimating unbiased  $f_{ho,z}$  is to utilize the relationship in Equation (3). This equation confirms that  $e_{t,y}$  is predominantly induced by  $f_{ho,z}$ . Therefore, by dividing  $e_{t,y}$  by the x-direction distance from CoM to the handle, vertical force estimation can be achieved without the influence of arbitrary payload additions. Ultimately, we estimate the pHRI wrench  ${}^B\mathbf{W}$  using the  ${}^B\hat{\mathbf{E}}_f$  and  ${}^B\hat{\mathbf{E}}_t$  signals from the DOB algorithms as follows:

$${}^B\hat{\mathbf{W}} = \begin{bmatrix} \hat{f}_{ho,x} \\ \hat{f}_{ho,y} \\ \hat{f}_{ho,z} \\ \hat{e}_{t,z} \end{bmatrix} = \begin{bmatrix} \hat{e}_{f,x} \\ \hat{e}_{f,y} \\ -\hat{e}_{t,y}/(x_h - x_c) \\ \hat{e}_{t,z} \end{bmatrix}. \quad (8)$$

3) *Overall system model*: Fig. 4 shows that  ${}^B\mathbf{H}_t$  and  ${}^B\mathbf{H}_f$ , introduced by the human operator, serve as the exclusive inputs

to the overall system, while  ${}^G\mathbf{q}$  and  ${}^G\mathbf{X}$  stand as the ultimate outputs. Notably, all the interconnecting systems between them are in a closed-loop configuration. Hence, assuming that the roll and pitch orientation of the Palletrone are kept close to zero thanks to the DOB, the relationship between the pHRI wrench  ${}^B\mathbf{W}$  and outputs  ${}^G\mathbf{X}$  and  $\psi$  can be expressed as follows:

$$\begin{bmatrix} {}^G\mathbf{X} \\ \psi \end{bmatrix} = \text{diag}(G_h, G_h, G_v, G_r^y) {}^G R_B(\mathbf{q}) {}^B\mathbf{W} + \begin{bmatrix} \mathbf{0}_{2 \times 1} \\ G_g \\ 0 \end{bmatrix} g, \quad (9)$$

where

$$\begin{cases} G_h(s) = \frac{\{x,y\}}{f_{ho,\{x,y\}}} = \frac{1+D_h}{(P_t^{-1}+D_h(P_t^{-1}-\bar{P}_t^{-1}))s^2+\bar{m}K_{tv}^h(K_{tp}^h+s)} \\ G_v(s) = \frac{z}{f_{ho,z}} = \frac{1+\bar{m}K_{tv}^v K_{tp}^v K_{adm}^v}{(P_t^{-1}+Q_t^v(\bar{P}_t^{-1}-P_t^{-1}))s^2+\bar{m}K_{tv}^v(K_{tp}^v+s)} \Gamma(s) \\ G_r^y(s) = \frac{\psi}{e_{t,z}} = \frac{1+D_r^y}{(P_{r3}^{-1}+D_r^y(P_{r3}^{-1}-\bar{P}_{r3}^{-1}))s+\bar{J}_3 K_{rv}^y(K_{rp}^y+s)} \\ G_g(s) = \frac{z}{g} = \frac{P_t^{-1}+Q_t^v(P_t^{-1}-\bar{P}_t^{-1})-P_t^{-1}}{((P_t^{-1}+Q_t^v(\bar{P}_t^{-1}-P_t^{-1}))s^2+\bar{m}K_{tv}^v(K_{tp}^v+s))} \\ D_h(s) = Q_t^h(\bar{m}K_{tv}^h K_{tp}^h K_{adm}^h - 1) \\ D_r^y(s) = Q_r^y(\bar{J}_3 K_{rv}^y K_{rp}^y K_{adm}^y - 1) \\ \Gamma(s) = \frac{\hat{f}_{ho,z}}{f_{ho,z}} = \frac{\hat{e}_{t,y}}{e_{t,y}} = \frac{Q_r^p(\bar{P}_{r2}^{-1}s+\bar{J}_2 K_{rv}^p(K_{rp}^p+s))}{Q_r^p(\bar{P}_{r2}^{-1}-P_{r2}^{-1})s+\bar{J}_2 K_{rv}^p(K_{rp}^p+s)} \end{cases} \quad (10)$$

In this context,  $G_{\{h,v\}}(s)$  is the transfer function linking pHRI forces and position, distinguishing between horizontal and vertical motions. Additionally,  $G_r^y(s)$  represents the transfer function connecting the lumped yaw input  $e_{t,z}$  with yaw attitude.  $G_g(s)$  is the transfer function relating gravity to the vertical position, and it becomes zero when considering  $Q_t^v(s)$  as 1, accounting for the constant characteristic of gravity.  $\Gamma(s)$  is the transfer function between the vertical pHRI force and its estimate, which is estimated from the pitch pHRI torque and its estimate. Furthermore, with  ${}^G R_B(\mathbf{q})$ , when roll and pitch are both zero, only yaw rotation is adjusted. In standard flight scenarios without rapid yaw motions, the impact of the rotation matrix between the pHRI wrench and the final pose response is minimal.

In the event of optimal operation of the DOB algorithm without cargo payload, we can treat  $Q_{(*)} \approx 1$  and  $P_{(*)} \approx \bar{P}_{(*)}$ . At this juncture, the nominal transfer functions in Equation (10) are expressed as,

$$\begin{cases} \bar{G}_{\{h,v\}}(s) \approx \left( \frac{K_{tv}^{\{h,v\}} K_{tp}^{\{h,v\}}}{s^2+K_{tv}^{\{h,v\}}s+K_{tp}^{\{h,v\}} K_{tp}^{\{h,v\}}} \right) K_{adm}^{\{h,v\}} \\ \bar{G}_r^y(s) \approx \left( \frac{K_{rv}^y K_{rp}^y}{s^2+K_{rv}^y s+K_{rp}^y K_{rp}^y} \right) K_{adm}^y \\ \bar{G}_g(s) \approx 0. \end{cases} \quad (11)$$

For ideal operational conditions within the DOB framework, the overall system becomes a structure comprising a dual-loop feedback control system involving position and velocity controllers alongside incorporating an admittance controller. Furthermore, the influence of gravity on altitude control is eliminated. Later, we can examine how the performance varies when loading arbitrary cargo masses, using Equation (11) as the reference model.

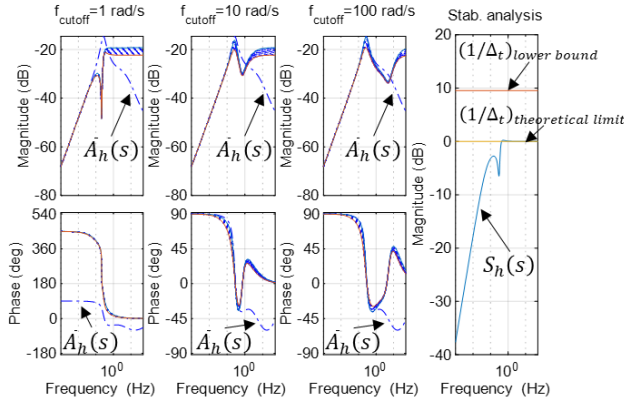


Fig. 5. **[Left three columns]** Bode plots showing the transfer function from horizontal force input to acceleration output, with varying cutoff frequencies. The dashed-dotted line represents the nominal model  $\bar{A}_h(s)$ , while other lines depict  $A_h(s)$ : responses with various payload masses. As Q-filter cutoff frequency increases, variation due to mass uncertainty decreases, aligning both magnitude and phase responses more closely with the nominal model. **[Last column]** Bode magnitude plot of  $S_h(s)$  and  $1/\Delta_t$  for stability analysis. To satisfy Equation (14),  $S_h(s)$  and  $1/\Delta_t$  should not overlap.

### C. Performance and Stability

When employing DOB for the admittance controller, the Q-filter serves two crucial functions in this study: canceling disturbances and estimating the pHRI wrench. Therefore, a meticulously designed Q-filter is essential to uphold targeted pHRI performance and system stability simultaneously. This subsection explores the influence of Q-filter design on system performance and stability in the presence of plant uncertainty, particularly considering cargo-induced variations in  $P_{\{t,r\}}(s)$ .

1) *Performance*: For clarity in exposition, we focus on horizontal translational motion analysis, but the same approach applies seamlessly to vertical and rotational motions.

Initially, plant uncertainty arises from the varying weight of the loaded cargo. We express the system in a multiplicative perturbation form, such as  $P_t(s) = \bar{P}_t(s)(1 + \Delta_t)$ , where

$$m_{max}^{-1}\bar{m} - 1 \leq \Delta_t \leq 0. \quad (12)$$

In contrast to classical multirotor control objectives, such as precise trajectory tracking [22], and effective disturbance rejection [23], evaluating the Palletrone pHRI performance is challenging because the haptic sensation of how well the system moves according to human intentions must be assessed. However, it is possible to analyze the resemblance between the transfer function linking pHRI force and the system's ultimate acceleration to the expected "push" and resulting "motion" from a classical Newtonian dynamics standpoint. This means we can judge the system's performance as the system motion becomes similar to the nominal behavior outlined in Equation (11). Thus, by comparing the magnitude and phase plots for the force-acceleration transfer functions in both the nominal and actual systems—represented by  $A_h(s) = G_h(s)s^2$  and  $\bar{A}_h(s) = \bar{G}_h(s)s^2$ , illustrating the connection between input force and output acceleration—we can assess the system's performance.

The first three columns of Fig. 5 represent the Bode plots of  $A_h(s)$  and  $\bar{A}_h(s)$  applied with the physical and control parameters in Table I used in the actual experiments. For  $A_h(s)$ ,

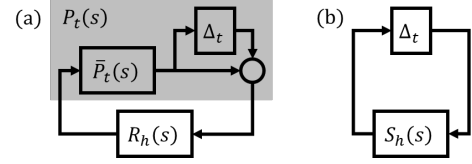


Fig. 6. **(a)** Perturbation model due to the uncertainty of  $P_t(s)$  in Fig. 4. **(b)** Model consolidating all components except  $\Delta_t$  from (a).

the response varies with changing mass, from the nominal mass  $\bar{m}$  to the maximum mass  $m_{max}$ . The Q-filter for the horizontal controller is designed as a first-order low pass filter  $Q_t^h(s) = 1/(s/f_{cutoff} + 1)$ , which meets the strictly proper system conditions outlined in Section III-A. The Bode plots exhibit responses corresponding to different Q-filter cutoff frequencies: 1 rad/s, 10 rad/s, and 100 rad/s (equivalent to 0.1592 Hz, 1.592 Hz, and 15.92 Hz, respectively). Given that disturbances induced by human input mainly consist of low-frequency components, analyzing responses in low-frequency regions reveals that a higher cutoff frequency brings the system response closer to the nominal. Moreover, increasing the cutoff frequency reduces the variation in system response caused by mass uncertainty. This suggests that elevating the cutoff frequency enhances the capacity of the DOB to maintain the nominal response against mass uncertainty, execute robust flight wrench control against human disturbances, and accurately estimate external forces. The phase response also approaches the nominal as the cutoff frequency increases, resulting in a smoother and non-peculiar sensation of system motion from a human perspective. Nevertheless, in practical experiments, constraints such as sensor noise limit the application of high cutoff frequency, necessitating iterative tuning to determine the highest feasible values.

2) *Stability*: In stability analysis, the Small-Gain Theorem [24] is utilized to address uncertainty arising solely from the system mass factor. Collapsing all control structures except  $P_t(s)$  shown in Fig. 4 and representing the collapsed system as block  $R_h(s)$  results in the perturbation model shown in Fig. 6-(a). Then, consolidating all components except the uncertainty  $\Delta_t$  into block  $S_h(s)$  yields the configuration illustrated in Fig. 6-(b). At this point,  $R_h(s)$  and  $S_h(s)$  are as follows:

$$\begin{cases} R_h(s) = (\bar{P}_t^{-1} - D_h^{-1})s^2 - K_{tv}^h(s + K_{tp}^h)D_h^{-1} \\ S_h(s) = \bar{P}_t R_h (1 - \bar{P}_t R_h)^{-1} \end{cases} \quad (13)$$

Following the claims of the Small Gain Theorem, the stability of the system is ensured when the following condition is satisfied [16].

$$\|S_h(s)\|_\infty < 1/\|\Delta_t\|_\infty \quad (14)$$

The Bode magnitude plot of the fourth column in Fig. 5 shows that the curve of  $S_h(s)$  satisfies the condition of Equation (14) by not intersecting with the curve of  $1/\Delta_t$ . According to Equation (12),  $\|1/\Delta_t\|_\infty$  has an upper bound of infinite size and a lower bound of  $\|1/(m_{max}^{-1}\bar{m} - 1)\|_\infty$ , and for an infinitely large  $m_{max}$ , it has an ultimate lower bound of 1, which is a theoretical limit of  $1/\|\Delta_t\|_\infty$ . Under the conditions outlined in Table I, the inequality condition is ensured for all possible mass variations until  $m_{max}$ , and the maximum weight can even be extended significantly: as much as the

TABLE I  
HARDWARE SPECIFICATIONS, PARAMETERS  
AND CONTROLLER GAINS FOR HORIZONTAL pHRI FLIGHT

On-board Computers & Sensors		Propulsion Systems	
Computer	LattePanda Delta (Intel Celeron N4100)	Servomotor	Dynamixel XL430-W250-T
Localization Sensor	Intel Realsense T265	Propeller	KDE Direct KDE-CF155-TP
IMU	Microstrain 3DM-GX5-25	Motor	KDE Direct KDE4215XF-465
H/W Param.	Value	H/W Param.	Value
$\bar{m}$	7.635 kg	$\bar{J}$	0.002 kg·m <sup>2</sup>
$m_{max}$	1.5 $\bar{m}$	${}^B\mathbf{P}_h$	[0.55 0.13 0] m
Controller	Value	Controller	Value
$K_{adm}^h$ (s)	$\frac{1}{0.5s^2+16s}$	$K_{tp}^h$ (s)	$\frac{0.7s^2+4s+0.01}{s}$
$K_{tv}^h$ (s)	$\frac{0.2s^2+0.9s+0.2}{s}$	$Q_t^h$ (s)	$\frac{1}{s/15+1}$

\*Note: The position and velocity controllers use PID feedback with transfer function numerators reflecting the D, P, and I gain coefficients in order.

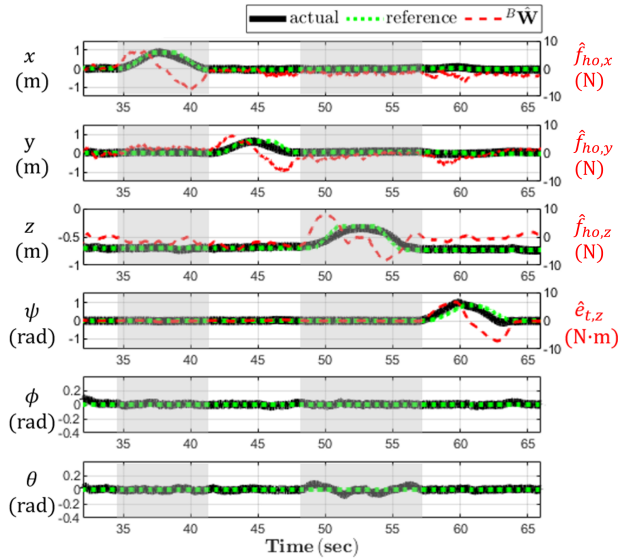


Fig. 7. [Experiment 1] pHRI flight performance validation of the Palletrone. The red dashed lines show estimated pHRI wrenches, green dots denote updated reference trajectories, and black solid lines represent actual platform motion. Independent control of three-dimensional translational and yaw motions is confirmed, with consistent roll and pitch attitudes during flight.

thrust capability allows. In the end, we confirm the stability of the system within the specified cargo weight.

#### IV. EXPERIMENT

In this section, we present three experiments aimed at evaluating the performance of the proposed Palletrone-based pHRI flight.<sup>1</sup> Hardware specifications, parameters, and controller gains constituting the pHRI flight experiment can be found in Table I.

##### A. 4-DOF pHRI Flight Performance Verification

The primary objective of the initial experiment was to assess the controllability of each motion channel using pHRI control wrenches, as depicted in Fig. 7. Rows one to four illustrate motion along the X, Y, and Z axes and yaw rotation, while

<sup>1</sup>An experiment video can be found at <https://youtu.be/8KQdqm8Ed4>.

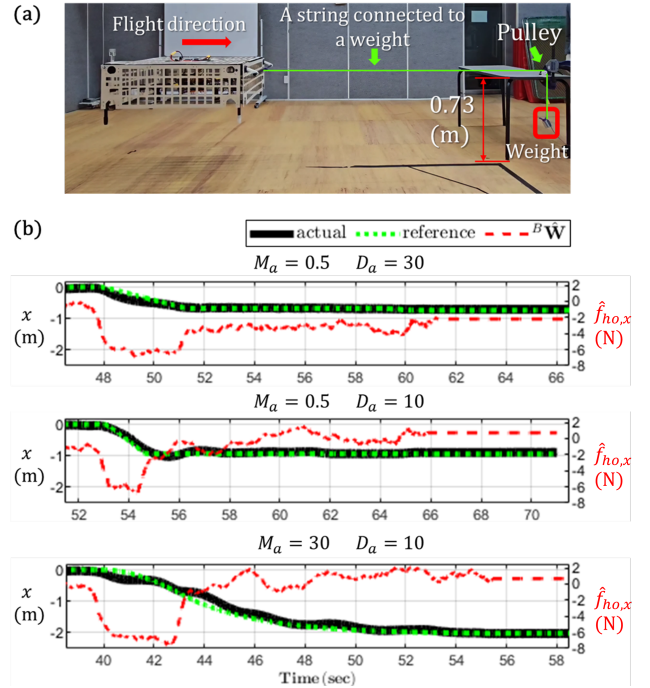


Fig. 8. [Experiment 2] Verification of the changes in flight characteristics resulting from admittance parameter tuning. (a) Experimental Setup: The Palletrone is connected to a pulley system with a weight. The weight is dropped from a fixed height to maintain consistent external force application on the Palletrone and uniform displacement. (b) Variations in motion characteristics resulting from changes in admittance controller parameters.

rows five and six showcase consistent roll and pitch attitude maintenance despite external pHRI wrenches. Analyzing the first four rows enables the observation of the estimated force and torque induced by the human operator, facilitating trajectory adjustments along the targeted motion channel where the force/torque was applied. Sequential application of forces and torques along each axis results in positional adjustments solely along the targeted motion channel while suppressing movements along other channels, demonstrating motion control independence.

##### B. Flight Characteristics Alteration with Admittance Tuning

The second experiment examined changes in flight behavior resulting from adjustments in admittance parameters outlined in Equation (5). In Fig. 8-(a), the experimental setup depicts the Palletrone tethered while a 1 kg weight hangs from the opposite end. As the experiment begins, the weight consistently descends from an initial height of 0.73m, ensuring the Palletrone experiences a steady force equivalent to the gravitational force of the weight during its horizontal flight over the same distance.

Fig. 8-(b) displays results from various admittance tunings. Comparing the first and second rows reveals that reducing  $D_a$  induces a more rapid change in position in response to the same force. On the other hand, increasing  $M_a$  from 0.5 to 30, as observed in the second and third experiments, notably slows down the motion due to the augmented virtual inertia. Nevertheless, in the third row, approximately after 43 seconds when the weight touches the ground, the Palletrone continues moving due to its substantial virtual inertia, even though the tether no longer maintains tension.

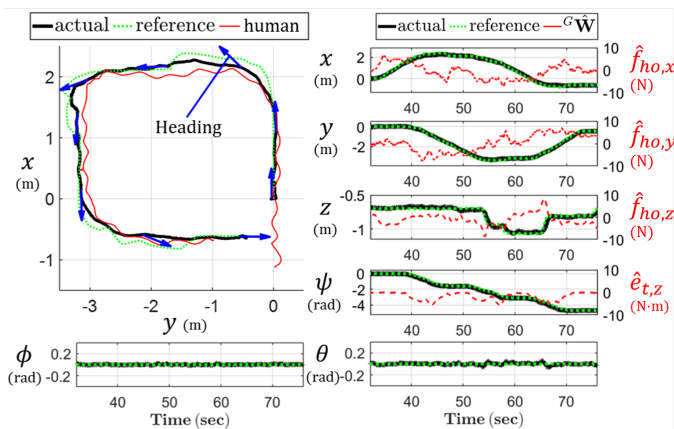


Fig. 9. [Experiment 3] Payload transportation by a person manipulating the Palletrone along an arbitrary path. Despite the complex application of pHRI wrenches to match the human trajectory, shown in the left figure, the reference trajectory of the Palletrone adjusts with stable roll and pitch attitudes.

Through these experiments, we validated the capability to tailor pHRI flight characteristics according to user preferences by adjusting virtual admittance properties based on the human operator's intentions.

### C. pHRI Flight with General Flight Scenario

The final experiment involved a person grasping the Palletrone, which was loaded with cargo weighing 2.93 kg. During this experiment, the human maneuvered the Palletrone along random trajectories. This experiment verifies the feasibility of general cargo transportation scenarios based on pHRI.

Fig. 9 illustrates a flight result. Despite the randomness of the trajectory, we observe that the motion of the Palletrone aligns with that of the humans, including the alignment of the heading angle and vertical motion, while maintaining a zero roll and pitch attitude. Ultimately, this experiment confirms that humans can intuitively operate the system as intended by its design, akin to maneuvering a shopping cart.

## V. CONCLUSION

In this study, we introduced a new aerial cargo transportation technique based on physical human-robot interaction using the novel Palletrone mUAV platform. This method enables flight according to physical human intention by estimating the force applied directly by the human to the platform and adjusting the trajectory accordingly. The proposed method also ensures stable human-robot interaction and cargo transportation by not tilting the platform, thanks to the fully-actuated flight characteristics of the Palletrone platform. We analyzed the impact of the human-operated pHRI control wrench on the system dynamics and used the DOB robust control algorithm to suppress undesired motion. Then, the admittance control structure was employed to implement pHRI, wherein the pHRI control wrench was estimated utilizing the internal signal within the DOB algorithm. We also conducted performance evaluations and stability analysis, along with three experiments validating the feasibility of human-robot interaction-based cargo transportation.

The current research assumes that disturbances applied to the system originate solely from humans, which may not

always hold true in general multirotor operating environments where external factors like wind or gusts can also introduce disturbances. Therefore, future research is required to selectively extract human intentions from various disturbances. Furthermore, the evaluation of current pHRI flight performance is primarily qualitative, relying on frequency response analysis via Bode plots; thus, establishing quantitative evaluation criteria and controlling the motion via optimization techniques to meet these criteria will be needed in future research.

## REFERENCES

- [1] Joubert, Niels, et al. "An interactive tool for designing quadrotor camera shots." *ACM Transactions on Graphics (TOG)* 34.6 (2015): 1-11.
- [2] Villa, Daniel KD, et al. "A survey on load transportation using multirotor UAVs." *Journal of Intelligent & Robotic Systems* 98 (2020): 267-296.
- [3] Cataldi, Elisabetta, et al. "Impedance control of an aerial-manipulator: Preliminary results." *IROS. IEEE*, 2016.
- [4] Suarez, Alejandro, et al. "Physical-virtual impedance control in ultralightweight and compliant dual-arm aerial manipulators." *IEEE Robotics and Automation Letters* 3.3 (2018): 2553-2560.
- [5] Afifi, Amr, et al. "Toward physical human-robot interaction control with aerial manipulators: Compliance, redundancy resolution, and input limits." *ICRA. IEEE*, 2022.
- [6] Allenspach, Mike, et al. "Human-state-aware controller for a tethered aerial robot guiding a human by physical interaction." *IEEE Robotics and Automation Letters* 7.2 (2022): 2827-2834.
- [7] Rajappa, Sujit, et al. "Design and implementation of a novel architecture for physical human-UAV interaction." *The International Journal of Robotics Research* 36.5-7 (2017): 800-819.
- [8] Augugliaro, Federico, et al. "Admittance control for physical human-quadrocopter interaction." *ECC. IEEE*, 2013.
- [9] Rashad, Ramy, et al. "Fully actuated multirotor UAVs: A literature review." *IEEE Robotics & Automation Magazine* 27.3 (2020): 97-107.
- [10] Mason, Matthew T. "Compliance and force control for computer controlled manipulators." *IEEE Transactions on Systems, Man, and Cybernetics* 11.6 (1981): 418-432.
- [11] Keemink, Arvid QL, et al. "Admittance control for physical human-robot interaction." *The International Journal of Robotics Research* 37.11 (2018): 1421-1444.
- [12] Schumacher, Marie, et al. "An introductory review of active compliant control." *Robotics and Autonomous Systems* 119 (2019): 185-200.
- [13] Fumagalli, Matteo, et al. "A modified impedance control for physical interaction of UAVs." *IROS. IEEE*, 2013.
- [14] Yüksel, Burak, et al. "Aerial physical interaction via IDA-PBC." *The International Journal of Robotics Research* 38.4 (2019): 403-421.
- [15] Hentzen, Daniel, et al. "Disturbance estimation and rejection for high-precision multirotor position control." *IROS. IEEE*, 2019.
- [16] Lee, Seung Jae, et al. "Robust acceleration control of a hexarotor UAV with a disturbance observer." *IEEE CDC. IEEE*, 2016.
- [17] W. Park, et al. "Design, Modeling and Control of a Top-Loading Fully-Actuated Cargo Transportation Multirotor." *IEEE Robotics and Automation Letters* 8.9 (2023): 5807-5814.
- [18] Esser, Patrick, et al. "IMU: inertial sensing of vertical CoM movement." *Journal of biomechanics* 42.10 (2009): 1578-1581.
- [19] Shim, Hyungbo, et al. "Yet another tutorial of disturbance observer: robust stabilization and recovery of nominal performance." *Control Theory and Technology* 14.3 (2016): 237-249.
- [20] Papadimitriou, Andreas, et al. "External force estimation and disturbance rejection for micro aerial vehicles." *Expert Systems with Applications* 200 (2022): 116883.
- [21] Tomić, Teodor, et al. "External wrench estimation, collision detection, and reflex reaction for flying robots." *IEEE Transactions on Robotics* 33.6 (2017): 1467-1482.
- [22] Dong, Wei, et al. "High-performance trajectory tracking control of a quadrotor with disturbance observer." *Sensors and Actuators A: Physical* 211 (2014): 67-77.
- [23] Lee, Seung Jae, et al. "Fully actuated autonomous flight of thruster-tilting multirotor." *IEEE/ASME Transactions on Mechatronics* 26.2 (2020): 765-776.
- [24] Kempf, Carl J., et al. "Disturbance observer and feedforward design for a high-speed direct-drive positioning table." *IEEE Transactions on control systems Technology* 7.5 (1999): 513-526.